ACS NANO

www.acsnano.org

ARTICLE

Structure Matters: Tailored Graphitization of Carbon Dots Enhances Photocatalytic Performance

Laura Morbiato, Lucia Cardo, Elisa Sturabotti, Pierangelo Gobbo,* Giacomo Filippini,* and Maurizio Prato*

Cite This: *ACS Nano* 2025, 19, 4887−4900

Read Online

ACCESS | Metrics & More | Article Recommendations | Supporting Information

ABSTRACT: **The chemical structure and photoredox properties of carbon dots (CDs) are not yet fully understood. However, it has been reported that, by carefully choosing the starting materials and tuning their synthesis conditions, it is possible to obtain CDs with different chemical structures and therefore different photocatalytic performance. For this work, a family of different CDs was synthesized in Milli-Q water *via* a microwave-assisted protocol, using citric acid and urea as precursors. The syntheses were carried out at different times and temperatures to assess the impact of the synthetic parameters on the photocatalytic properties of the final materials. After extensive and accurate purification, the photocatalytic abilities of a selected subset of CDs were tested by performing a photocatalyzed atom transfer radical addition reaction. Among the tested CDs, the best performing ones were found to be those synthesized at the highest temperature, which were the most graphitic. A number of different characterization techniques were then used to evaluate the degree of graphitization of CDs and to elucidate the origin of their different photocatalytic performance.**

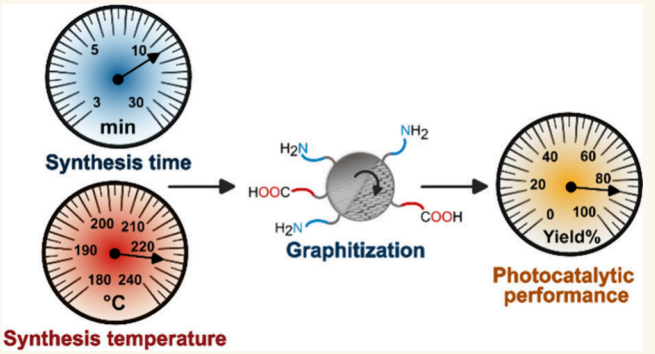

KEYWORDS: *carbon nanomaterials, graphitic carbon dots, synthesis optimization, tuned graphitization, photocatalysis, CD-based photocatalysts*

INTRODUCTION

Photocatalysis has stimulated strong interest within the scientific community because it offers the possibility of harnessing the power of visible-light to forge novel chemical bonds in an environmentally friendly manner.[1,2] In this context, over recent years, photoredox catalysis, involving the light-driven transfer of one electron from or to a suitable substrate, has become a key tool for the mild functionalization of organic compounds.[3] Interestingly, this approach allows for the effective production of highly reactive intermediates such as radicals and radical ions. These intermediates may then trigger unique reactivity pathways that are impossible to access under classical thermal conditions.[4] To date, the most widely used photoredox catalysts include expensive and often environmentally harmful polypyridyl complexes of ruthenium or iridium and organic dyes, which are generally used in relatively high catalytic loading (up to 30 mol %).[5] Nevertheless, it has recently emerged that these photocatalysts are not attracting industrial interest due to their limitations in terms of recovery and recycling and due to the tedious multiple step synthetic routes required for their synthesis.[6,7] For these reasons, extensive effort is still focused on the development of new effective nontoxic metal-free photoredox catalysts, that are recyclable and easy to synthesize.[3]

Carbon Dots (**CDs**) have gained increasing attention as viable metal-free alternatives to traditional photocatalysts, because they are easy to prepare, nontoxic and potentially recyclable.[8,9] They have recently been exploited to perform novel photodriven carbon−carbon and carbon−heteroatom bond forming transformations, overcoming some of the drawbacks of traditional photocatalysts.[4,10] From a structural point of view, **CDs** are intrinsic fluorescent core−shell-like particles with dimensions

Received: November 18, 2024
Revised: December 27, 2024
Accepted: December 30, 2024
Published: January 22, 2025

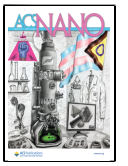

below 10 nm composed by an inner carbonaceous core and an outer shell of functional groups such as hydroxylic groups, carboxylic acids and amines (Figure 1a).[11,12] The combination

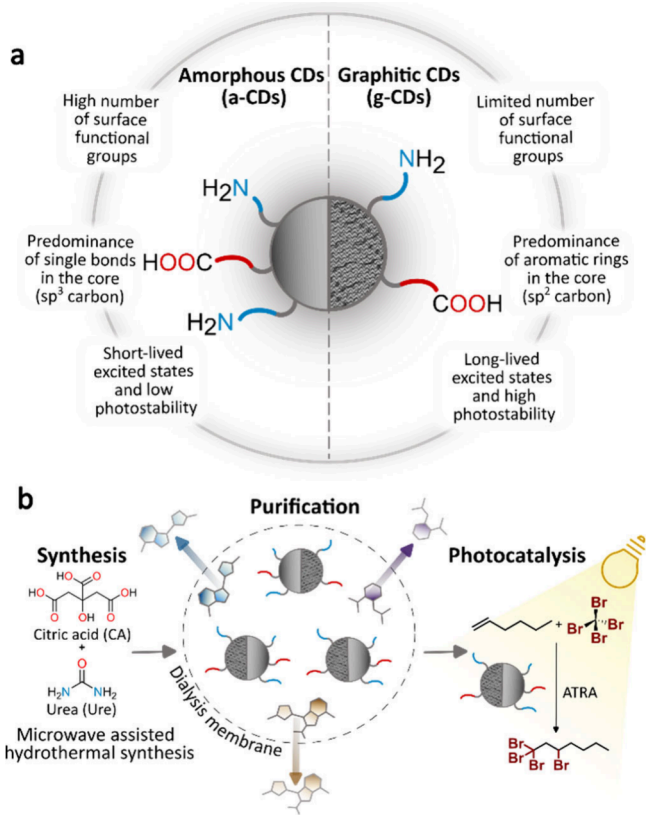

Figure 1. (a) Schematic representation of CD cores, highlighting surface functional groups and key characteristics. (b) CDs workflow from synthesis to photocatalytic application.

of properties imparted by both the core and the surface functional groups gives the **CDs** many interesting physicochemical properties, resulting in good catalytic and photocatalytic behavior and high chemical and photostability.[13−15] **CDs** can be obtained using a variety of inexpensive and readily available carbon-based precursors, using both *top-down* (from bulk materials to **CDs**) or *bottom-up* synthesis (from molecular precursors to **CDs**).[16] During the synthesis of these materials, however, multiple reaction pathways are possible.[17] Due to this, their synthesis generally provides the desired nanoparticles along with a number of molecular side-products and large carbon aggregates. It is worth mentioning that the photochemical properties of these byproducts can be easily confused with those of the **CDs**. For this reason, extensive purification of the nanoparticles is essential before their characterization and application.[18,19] However, despite the recent advancements in the development of suitable techniques for the characterization of **CDs**, the correlation between the **CD** structure and their photocatalytic performance still remains an important challenge in the field.[20,21]

Recently, nuclear magnetic resonance (NMR) spectroscopy has emerged as an effective tool to assess the presence of molecular impurities in the **CD** solutions.[22] Because of their polymeric and heterogeneous nature, the ^{1}H NMR spectra of clean **CDs**, generally, present broad and unresolved peaks. This behavior is reasonably related to the fact that protons entrapped in complex nanostructures encounter different magnetic environments and slow rotations.[23] On the other hand, the presence of sharp signals in the ^{1}H NMR profile is related to the persistence of low molecular weight molecules, hence indicating that further purification is required.[24] In addition, Diffusion-Ordered Spectroscopy (DOSY) can be used to provide insights into the purity and polydispersity of the analyzed samples. Furthermore, the analysis of the diffusion coefficients retrieved by DOSY is a viable method to gain information on the

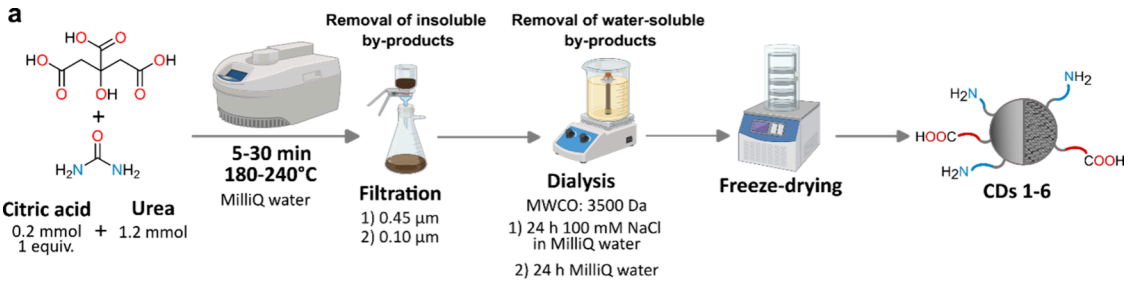

b

CDs summary

Entry	*CDs type*	*Synthesis time (min)*	*Synthesis temperature (°C)*
1	**CDs-1**	**5**	180
2	**CDs-2**	**10**	180
3	**CDs-3**	**30**	180
4	**CDs-4**	10	**200**
5	**CDs-5**	10	**220**
6	**CDs-6**	10	**240**

c

Figure 2. (a) Workflow for the synthesis and purification of CDs. (b) Table summarizing the conditions used for the synthesis of CDs. (c) Image showing the typical aspect of a sample of purified and lyophilized CDs. Specifically, the samples in the image is CDs-5.

https://doi.org/10.1021/acsnano.4c16538
ACS Nano 2025, 19, 4887−4900

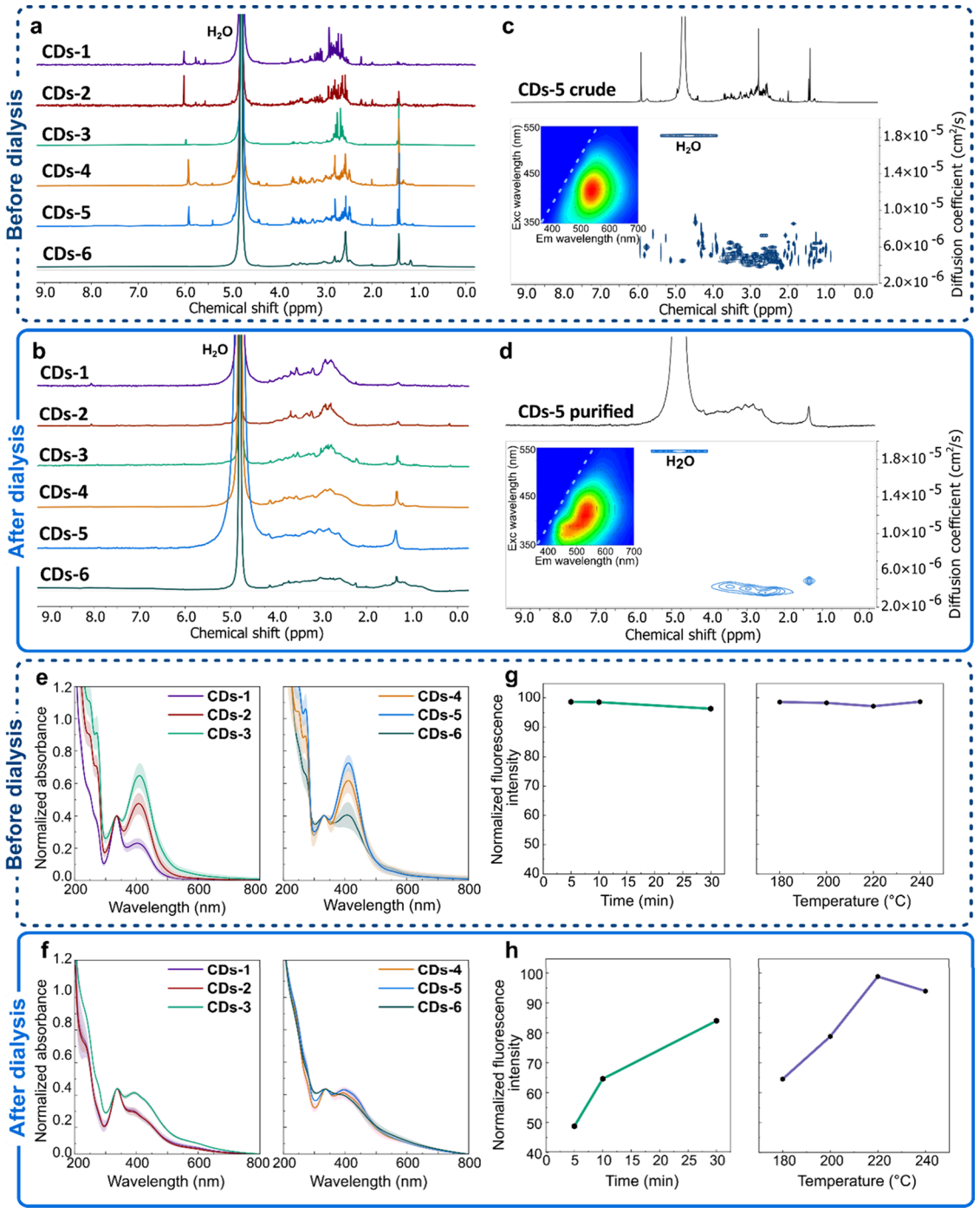

Figure 3. (a) ^{1}H NMR spectra of CDs 1-6 reaction crude acquired in D_2O and calibrated against residual water. (b) ^{1}H NMR spectra of purified CDs 1-6 acquired in D_2O and calibrated against residual water. (c) DOSY spectrum of CDs-5 reaction crude acquired in D_2O and calibrated against residual water. The inset reports the emission map of the same sample acquired in Milli-Q water. The fluorescence intensities of the emission map were normalized between 0 (blue) and 100 (red color). The dashed diagonal line inside the emission map limits the region of real values acquired during the experiments. (d) DOSY spectrum of purified CDs-5 acquired in D_2O and calibrated against residual water. The inset shows the emission map of the same sample acquired in Milli-Q water. The fluorescence intensities of the emission map were normalized between 0 (blue color) and 100 (red color). The dashed diagonal line inside the emission map limits the region of real values acquired during the experiments. (e) Absorption spectra of CDs 1-6 reaction crudes acquired in Milli-Q water. All the spectra were normalized at 335 nm. Error bands are the standard deviation over three replicas. (f) Absorption spectra of purified CDs 1-6 acquired in Milli-Q water. All the spectra were normalized at 335 nm. Error bands are the standard deviation over three replicas. (g) Plot showing no changes in the normalized fluorescence intensity (λ_{ex} = 410 nm; λ_{em} = 530 nm) as a function of the synthesis time (left, green plot, crude samples CDs 1-3), or as a function of the temperature (right, purple plot, crude samples CDs 4-6). All samples were analyzed in Milli-Q water. (h) Plot showing changes in the normalized fluorescence intensity (λ_{ex} = 410 nm; λ_{em} = 530 nm) as a function of the synthesis time (left, green plot, purified samples CDs 1-3), or as a function of the temperature (right, purple plot, purified samples CDs 4-6). All samples were analyzed in Milli-Q water.

https://doi.org/10.1021/acsnano.4c16538
ACS Nano 2025, 19, 4887−4900

dimension of the analyzed species, as the smaller the diffusion coefficient is, the larger the analyte is.[25,26]

Since their discovery back in 2004, the nomenclature and exact classification of **CDs** have been the object of debate.[27] In spite of this, in most of the cases, **CDs** are classified based on the structure of their core.[28] As reported in Figure 1a, according to this classification, **CDs** are grouped in two main classes: (*i*) **CDs** with a predominantly amorphous core (**a-CDs**), and (*ii*) **CDs** with a predominantly graphitic core (**g-CDs**).[29,30] However, in many cases, **CDs** have a core that possesses a structure that is a hybrid between the two situations. This implies the possibility of tuning the **CD** graphitization to modulate their physicochemical properties.[31]

The degree of graphitization of **CDs** can be investigated by Transmission Electron Microscopy (TEM) imaging and X-ray diffraction (XRD). In particular, TEM allows for the visualization of the lattice fringes in the core of the **CDs** (if present), while XRD is a widely used nondestructive method to study carbon materials and investigate their graphitic structure.[32,33]

In the present work, citric acid (CA) and urea (Ure) were employed as the precursors to synthesize six samples of nitrogen-doped **CDs** with different degrees of graphitization in their inner core. Subsequently, those **CDs** that were obtained in sufficiently high yields after purification were tested as photocatalysts.

As a proof of concept, we tested the abilities of our **CDs** to photocatalyze the atom transfer radical addition (ATRA) reaction between 1-hexene and carbon tetrabromide to yield the final product 1,1,1,3-tetrabromoheptane (Figure 1b).[34,35] According to the reaction output, the conditions used for the synthesis of **CDs** were found to have an effect on their photocatalytic performance. In fact, the best performing **CDs** were those synthesized at the highest temperature and, therefore, the most graphitic. To the best of our knowledge, this work provides the first example of how tailoring the degree of graphitization of **CDs** results in the enhancement of their photocatalytic abilities. Furthermore, our findings pave the way for the widespread application of **CDs** in photocatalysis by providing a viable method to study their structure−photocatalytic property relationship. This will benefit the engineering of a new generation of inexpensive photocatalysts, thus ensuring the possibility of expanding their application to synthetic, industrial and naturally relevant photochemical transformations.

RESULTS AND DISCUSSION

Synthesis and Purification of CDs. To synthesize the **CDs**, the object of this work, different operative conditions were employed. In particular, the synthesis of **CDs** (Figure 2a) was performed at different times and temperatures as indicated in Figure 2b, to evaluate the impact of these two parameters on the graphitization degree. Figure 2c shows the typical aspect of purified **CDs** obtained.

To date, the synthetic pathway that leads to the formation of **CDs** is not fully understood.[30] However, several mechanisms have been proposed.[17,33,36] Typically, by employing citric acid and urea as starting materials, the reaction starts with condensation that produces small molecules, most of which are fluorescent. Thereafter, as the reaction conditions become harsher, the formation of molecular fluorophores increases, followed by their aggregation into polymeric structures up to the formation of the first dots. These polymeric dots can then react to form **CDs** with an amorphous core (**a-CDs**) and a variety of functional groups on their surfaces. Subsequently, if the temperature is sufficiently high and the synthesis duration is long enough, the amorphous cores of the **CDs** graphitize, yielding graphitic **CDs** (**g-CDs**). **g-CDs** are usually smaller compared to the amorphous ones, and with a reduced number of functional groups on their surfaces.[11] Finally, if the temperature is increased further (beyond 220 °C for the systems object of this work), the yield of **CDs** decreases drastically and highly carbonized carbon-based materials and insoluble molecular aggregates are formed.

The removal of the molecular side-products produced during the synthesis and the use of clean materials is crucial to avoid erroneous attributions of **CD** optoelectronic properties.[24,37] In fact, the bright emission of these fluorescent molecular side-products may overlap with the modest emission of **CDs**.[19,38] Unfortunately, in most of the protocols for the synthesis of **CDs**, the purification step is underestimated or completely missing.[39,40] It is therefore crucial to implement any synthetic protocol with a suitable purification step.[24,41]

As the **CDs** synthesized for this work were water-soluble, the protocol chosen for their purification was a filtration to remove the insoluble byproducts, followed by dialysis of the soluble fraction. To find the best dialysis conditions, dialysis membranes with three different molecular weight cutoffs (MWCO) were employed: 100−500 Da, 500−1000 and 3500 Da (Figure S1). After dialysis, NMR spectroscopy was used to assess the presence of molecular compounds in the **CD** fraction.[22] In the ^{1}H NMR spectra of the dialyzed **CDs**, peaks of molecular side-products were still present, showing that none of the three dialysis protocols was effective for the purification of **CDs** (Figure S1a−c). We hypothesized that the incomplete purification was due to electrostatic interactions between **CDs** and their side-products. For this reason, along with the use of a membrane with 3500 Da MWCO, 100 mM NaCl was added to the dialysis water. The high MWCO, together with the presence of the salt, was effective in removing the ionic interactions, thus facilitating the permeation of the side-products through the dialysis bags.

The ^{1}H NMR spectra of the so-purified **CDs** (Figure S1d) confirmed the absence of discrete molecules and therefore the validity of the method. Once the best conditions were found, this purification protocol was applied to all of the batches of **CDs** (i.e., **CDs 1-6**, Figure 2b).

As reported in Figure 3a, the ^{1}H NMR spectra of **CDs 1-6** reaction crudes exhibit sharp molecular peaks that were not present in the spectra of the purified **CDs** (Figure 3b and Figure S2). Besides the purity of the samples, NMR spectroscopy can also be used to obtain some structural information about the chemical nature of the **CDs**. In detail, the ^{1}H NMR spectra of purified **CDs 1-6** presented peaks mostly centered between 2 and 4 ppm, compatible with the presence of protons (e.g., CH; CH_2 and CH_3) linked to different functional groups (such as N−**CH**; O=C−**CH**; C−**CH**; N−C−**CH**; and O−**CH**). On the contrary, the peaks of aromatic or heteroaromatic protons that we expected to find at chemical shifts between 7 and 9 ppm could not be detected by NMR spectroscopy due to the highly condensed nature of the **CD** cores.

The purity of **CDs 1-6** was further confirmed by the DOSY characterization.[26] In fact, by comparing the DOSY spectra of **CDs-5** reaction crude (Figure 3c) and purified **CDs-5** (Figure 3d), it is clear that the **CDs** are not contaminated by molecular impurities, and diffuse as a fairly monodisperse material. This trend was observed for all of the **CDs** under study (^{1}H NMR and DOSY spectra of all the analyzed batches are in Figure S3)

https://doi.org/10.1021/acsnano.4c16538
ACS Nano 2025, 19, 4887−4900

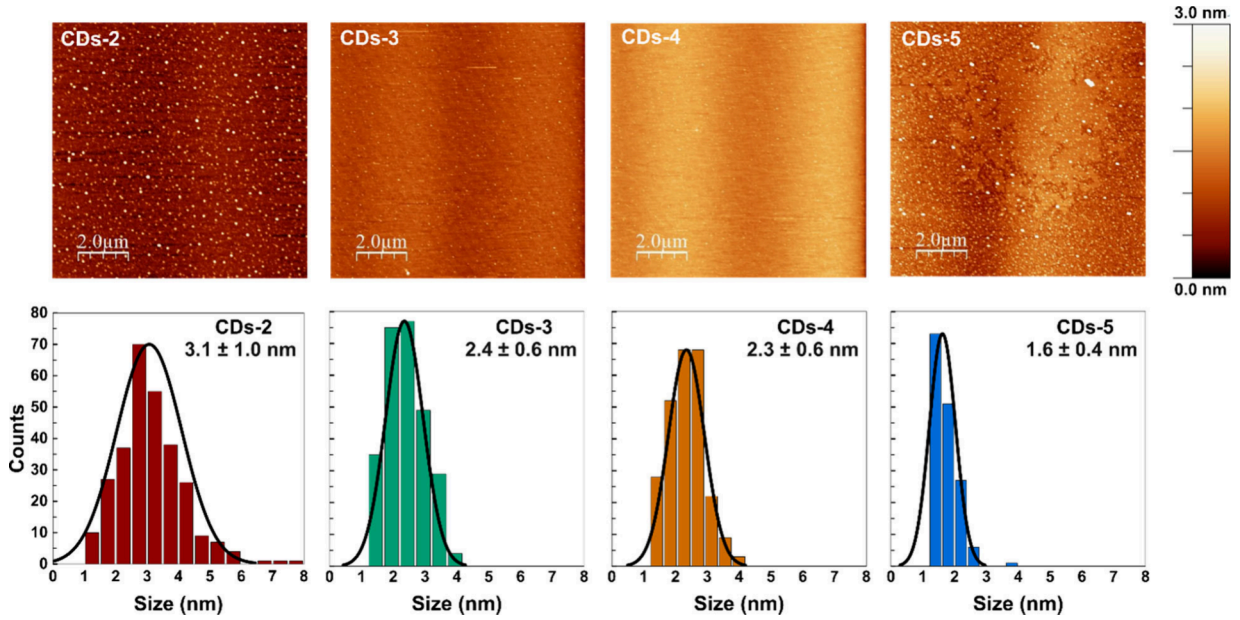

Figure 4. AFM images (top) and size analysis (bottom) of CDs 2-5 drop-casted from Milli-Q water on a mica substrate. In the AFM images, false color scale refers to CD heights on the *z* axis. Size distribution plots were fitted with a Gaussian function. The errors reported are the standard deviations of the distributions.

indicating the suitability of the purification method employed. Notably, in good accordance with the literature, the comparison of the diffusion coefficients of **CDs 1-6** seemed to indicate that the harsher reaction conditions resulted in smaller nanoparticles (Figure S3g).[38]

Following these initial general assessments *via* NMR spectroscopy, absorption and emission spectra of **CDs 1-6** were recorded. Typically, the absorption spectra of **CDs** show strong absorbance in the UV region, with a tail in the visible region. The intensity and position of the absorption bands may depend on the degree of graphitization of the cores of **CDs**, and on the chemical nature of their surface functional groups.[42,43] In addition, **CDs** also generally present an excitation-dependent fluorescence emission that can be tuned over the entire visible range.[19,44,45]

To evaluate the impact of the synthetic parameters and to assess the influence of the molecular side-products on the optical properties of the **CDs**, absorption and emission spectra of **CDs 1-6** were acquired before and after purification. In addition, a sample of dialysis water from each synthesized batch was collected and analyzed after 3 and 24 h of dialysis (Figures S4–S10). The results were used as an indirect method to provide insights into the chemical nature of the synthesis side-products and on the purification process and helped identify the best dialysis protocol.

The UV–vis spectra of the **CD** reaction crudes (Figure 3e) present two main peaks at ≈335 and ≈407 nm. Notably, the second peak became more pronounced with the increase of the synthesis time and temperature, consistently with an increased presence of conjugated aromatic systems that absorbed in the visible region. These aromatic systems can be found in the **CD** cores, but also as synthesis byproducts.[41,46] The presence of visible-light-absorbing aromatic byproducts was further supported by the presence of two other absorption bands (≈248 nm and ≈270 nm) in the reaction crudes of **CDs 2-5**, ascribable to molecular impurities.[47] These bands were less pronounced in **CDs-1** and **CDs-6**, and they were not present in the purified samples (Figure 3f). In fact, after purification, the absorbance at ≈335 nm was still present, proving to be directly ascribable to **CDs**, while the peaks at ≈248 and ≈270 nm disappeared, indicating that they were correlated to molecular side-products. Furthermore, the peak at ≈407 nm decreased significantly (the contribution of molecular side-products was removed) and split in two (≈405 and ≈425 nm) revealing the real absorption profile of **CDs**. In detail, after purification, the UV–vis spectra of **CDs 3-5** showed a detectable bathochromic shift and a hyperchromic effect compared to **CDs-2** that were related to an increased presence of highly conjugated organic clusters in their core, i.e. to an increased graphitization. In fact, it is well-known from the literature that an increased graphitization and conjugation of aromatic molecules results in a bathochromic shift to the visible region of the UV–vis spectra (see Appendix 1 for the numerical values of extinction coefficient spectra of **CDs 2-5**).[48]

To analyze the emission properties of **CDs**, the emission maps of the reaction crudes for samples **CDs 1-6** were acquired (Figure 3c-d insets; Figure S9a-c and Figure S10a-c). To complete the study, the emission maps of **CDs** purified with all the screened dialysis MWCO were also recorded and analyzed (Figure S9d-l and Figure S10d-l). All the emission maps of both reaction crudes and purified samples were normalized between 0 and 100, and the normalized fluorescence intensity at 530 nm (λ_{ex} = 410 nm) was plotted as shown in Figure 3g-h. This comparison shows that before dialysis the emission was substantially the same in all the analyzed samples and was not excitation dependent, confirming to be mostly caused by molecular side-products (Figure 3c inset).[36,47] Interestingly, as reported in Figure 3h, the increase of the synthesis time and temperature resulted in an increased fluorescence emission at 530 nm, compatible with an increased graphitization of the **CD** cores.[42,49] The inversion of the trend above 220 °C was ascribed to an excess of graphitization induced by the high temperatures, which yielded low-emission and highly carbonized **CDs**. After purification, the emission profile of the **CDs** changed, and the

https://doi.org/10.1021/acsnano.4c16538
ACS Nano 2025, 19, 4887–4900

excitation-dependent emission appeared in all the batches (Figure 3d inset; Figure S9m-o and Figure S10m-o).

Purified **CDs** obtained with the highest mass yields (Figure S11) and selected for photocatalysis tests (**CDs 2-5**) were first examined by Atomic Force Microscopy (AFM) imaging. This analysis showed **CDs** with a round shape and a rather narrow size distribution, with an average vertical (z) size between 2 and 4 nm. It is worth mentioning that the mean diameter of samples **CDs-5** was smaller compared to that of the other **CDs**. This was consistent with the results obtained with DOSY experiments and confirmed that an increase in synthesis temperature induced a reduction of **CD** size (Figure 4).

Impact of the Synthesis on the Photocatalytic Abilities of CDs. The reaction between 1-hexene (**1a**) and carbon tetrabromide (**2a**) was chosen as a model reaction to test the photocatalytic abilities of **CDs 2-5** (Figure 5a). The selected solvent to carry out the reaction was acetonitrile (MeCN), due to its (*i*) optical properties (*ii*) excellent photostability and (*iii*) ability to solubilize both the olefin (**1a**) and the radical source (**2a**). A Kessil lamp was used as the visible light source (λ_{max} = 456 nm, 50 W, Irradiance = 200 mW cm^{-2}).[34,50] See Figure S12 for a detailed explanation of the experimental setup.

Under these reaction conditions **CDs 2-4** resulted in progressively better, but moderate yields (entries 1−3), while **CDs-5** led to the formation of product **3a** in good yield (entry 4). To gain further insight into the reaction mechanism, we also performed some control experiments. Specifically, no reaction occurred without the photocatalyst (entry 5), or without light irradiation (entry 6), confirming that this reaction requires the presence of both light and a photocatalyst to be performed. We also carried out the reaction in the presence of air (entry 7) and, as reported in entry 8, in the presence of 2,2,6,6-tetramethyl-1-piperidinyloxy (TEMPO). In the first case, no reaction occurred, while in the latter the reaction did not yield the desired product **3a**. These results confirmed that the reaction proceeds *via* the formation of radical intermediates (Figure 5b).

From a mechanistic point of view, **CDs-5** may directly reach an electronically excited state (**CDs-5***) upon light absorption. **CDs-5*** is then capable to trigger the formation of the electron-deficient radical **Ia** through the reductive cleavage of **2a**, which is an easily reducible radical precursor (E_{red} = −0.31 V vs SCE), *via* a single electron transfer (SET) mechanism (Figure 5b).[51] To corroborate this hypothesis, we performed a series of Stern−Volmer quenching studies (Figure S13). First, the emission spectrum of **CDs-5** was recorded after excitation at λ = 456 nm (maximum emission at λ = 540 nm). Afterward, we observed that **2a** effectively quenched the emission and therefore the excited state of the nanoparticles. In our studies, a linear Stern−Volmer correlation was observed (Stern−Volmer constant, K_{sv} = 0.01 mM^{-1}), which means that a single type of quenching phenomenon occurs, likely *via* a SET mechanism (see Figure S14).[52] These studies suggested that a photoinduced SET from **CDs-5*** to **2a** could be viable at ambient temperature. Then, radical **Ia** reacts with the C=C bond within substrate **1a**, and the catalysis eventually evolves to the final desired ATRA product (**3a**).

After the reactions, **CDs-5** were recovered by extraction with water/ethyl acetate, followed by freeze-drying of the aqueous phase. The recyclability of **CDs-5** was verified over four cycles obtaining good reaction yields (Figure 5c). The partial loss of activity observed over the fourth cycle could be attributed to both mass loss during **CD** recovery and partial degradation of the **CDs**. In detail, as reported in Figure S17, the ^{1}H NMR spectrum of **CDs-5** after catalysis showed some differences compared to that of the pristine ones. These differences were ascribed to small changes in the chemical structure of the **CDs** due to photobleaching and to possible irreversible radical side-reactions occurring during catalysis. On the other hand, the UV−vis spectrum (Figure S18), the emission map (Figure S19) and the FT-ATR spectrum (Figure S20) of **CDs-5** after catalysis

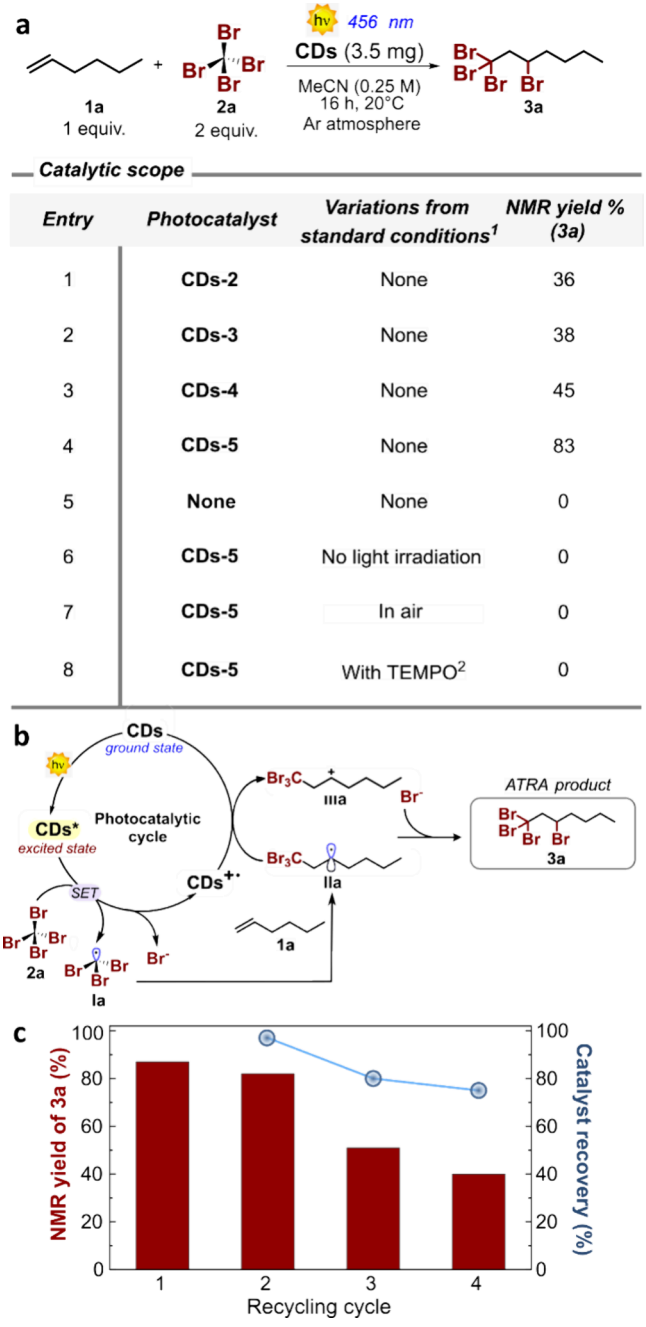

Figure 5. (a) Scheme showing the photocatalytic proof-of-concept reaction (top) and table showing optimization studies and control experiments (bottom). (b) Scheme showing the proposed reaction mechanism. (c) Plot showing the relationship between the reaction yield over four cycles using CDs-5 as the photocatalysts and their mass recovery. [1]Standard conditions: MeCN 0.25 M; inert argon atmosphere; 3 cycles of degassing (5 min each), [2]2,2,6,6-Tetramethyl-1-piperidinyloxy (1 equiv). NMR yield was calculated using 1,3,5-Trimethoxybenzene as the internal standard.

https://doi.org/10.1021/acsnano.4c16538
ACS Nano 2025, 19, 4887−4900

were comparable with those of the pristine **CDs**, confirming that their main structure remained substantially the same.

Stimulated by these results, we carried out a more in-depth characterization of the **CDs** to study their structure−property relationships and to understand their photocatalytic abilities. First, to complete the characterization of their absorption properties, the solid-state absorption of the **CDs** powder was recorded. The results reported in Figure S21 confirm that the absorption properties of **CDs** were essentially the same as those acquired in solution. The ability of **CDs 2-5** to absorb light at the wavelength used for the catalytic evaluations (456 nm) was then evaluated by calculating their extinction coefficients.[53] As expected, **CDs-5** were revealed to be the **CDs** with the highest extinction coefficient (9 mL mg^{-1} cm^{-1}) among the tested **CDs**, compatible with an increased conjugation in their core (Figure 6a and Figure S22). Appendix 1 reports the numerical values of the extinction coefficient spectra of **CDs 2-5**.

In addition to the absorption properties, another key parameter of a good photocatalyst is its ability to form long-lived excited states. Figure 6b reports the lifetimes of the excited states of **CDs 2-5**.[54−57] The results obtained were consistent with the literature and confirmed the ability of **CDs** to generate longer-lived excited states as a result of increased synthesis times and temperature. This seems compatible with an increased graphitization of the **CD** cores that facilitates electron trapping within the carbon sp^2 domains, yielding **CDs** able to generate excited states with progressively longer lilfetimes.[55] In particular, the excited state lifetimes of **CDs-5** (best catalytic performance) resulted to be $\tau_1 \approx 2$ ns and $\tau_2 \approx 10$ ns, which are significantly higher than those of **CDs-2** (worse photocatalytic performance). The fitting curves of the raw data for the calculation of the lifetimes of **CDs 2-5** are reported in Figure S23.

To prove the initial assumption that by tuning the reaction conditions, it is possible to tune the graphitization of **CDs**, the latter were examined by TEM imaging and XRD. TEM images of **CD 2-5** are reported in Figure 7a. From the analysis of the images, it emerged that **CDs-5** (bottom right image) present a clear lattice pattern with an interlayer spacing of 0.21 nm. According to literature, this value is common for **CDs** with a graphitic core, and it is compatible with a higher amount of sp^2 carbon atoms over carbon sp^3.[58] On the other hand, none of the other **CDs** showed clear lattice fringes, confirming the hypothesis that the conditions of their synthesis were not harsh enough to induce the graphitization of their core. In addition, the statistical analysis of the **CD** dimensions obtained by TEM showed that the nanoparticles were quite monodisperse, with an average size between 2 and 4 nm (Figure 7b). It is worth noting that the diameters of **CDs** (obtained by TEM) and the heights of **CDs** (obtained by AFM) were in the same range, confirming that **CDs** were quasi-spherical nanoparticles. In addition, both techniques revealed the same trend of size reduction as a function of synthesis time and temperature. The comparison between TEM imaging and DOSY diffusion coefficients highlighted that the **CD** dimensions and their diffusion coefficients were inversely proportional (Figure 7c), confirming the trend.

The crystalline structure of **CDs** was also investigated by XRD diffraction. The XRD patterns of all of the analyzed **CDs** exhibited similar broad peaks typical of polymeric structures and compatible with their partially disordered structure. Concerning the **CD** structure, a peak centered at $2\theta = 27°$, corresponding to the (002) plane of graphite, could be individuated in the diffractograms of **CDs 3-5** (Figure S24). This peak, which

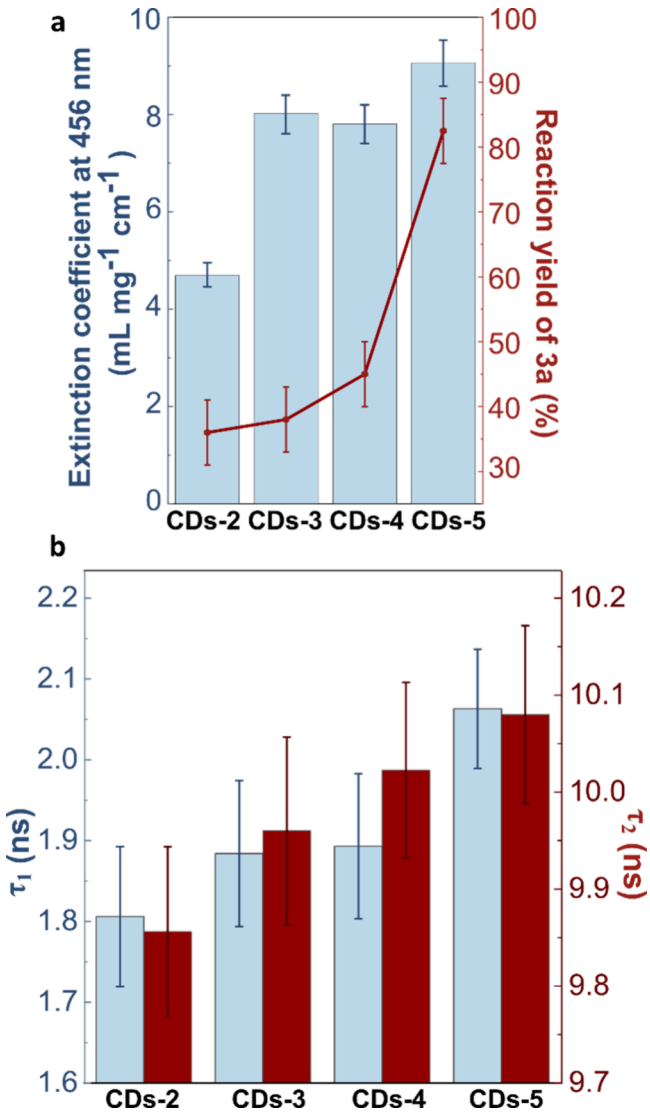

Figure 6. (a) Plot highlighting the relationship between the extinction coefficient of CDs 2-5 (calculated in mg mL^{-1} at 456 nm) and the reaction yield of product 3a. For the calculation of the extinction coefficients, the absorption spectra were acquired in Milli-Q water. Error bars correspond to the standard deviation over three replicas. (b) Plot reporting the excited states lifetimes of CDs 2-5. The measurements were carried out in Milli-Q water. The values were retrieved by biexponential fitting of the raw data. Error bars correspond to the fitting confidence errors.

corresponded to a *d*-spacing of about 0.35 nm, reflected the presence of sp^2-hybridized carbon atoms arranged in a graphitic lattice similar to that of the bulk graphite. This peak was not present in **CDs-2** confirming their poor crystalline nature (Figure 7d).[20,59,60] Moreover, all the XRD patterns showed a high background intensity, which was ascribed to the presence of highly disordered materials in the form of amorphous carbon.[32] Interestingly, this background intensity decreased from **CDs-2** to **CDs-5**, indicating their progressively increasing graphitization (Figure 7e). These findings were in good agreement with the TEM images (Figure 7a-c) and seemed to indicate that **CDs-5** were the most graphitized among the **CDs** analyzed. A smaller degree of graphitization was also present in the cores of **CDs-3** and **CDs-4** (Figure S24).

https://doi.org/10.1021/acsnano.4c16538
ACS Nano 2025, 19, 4887−4900

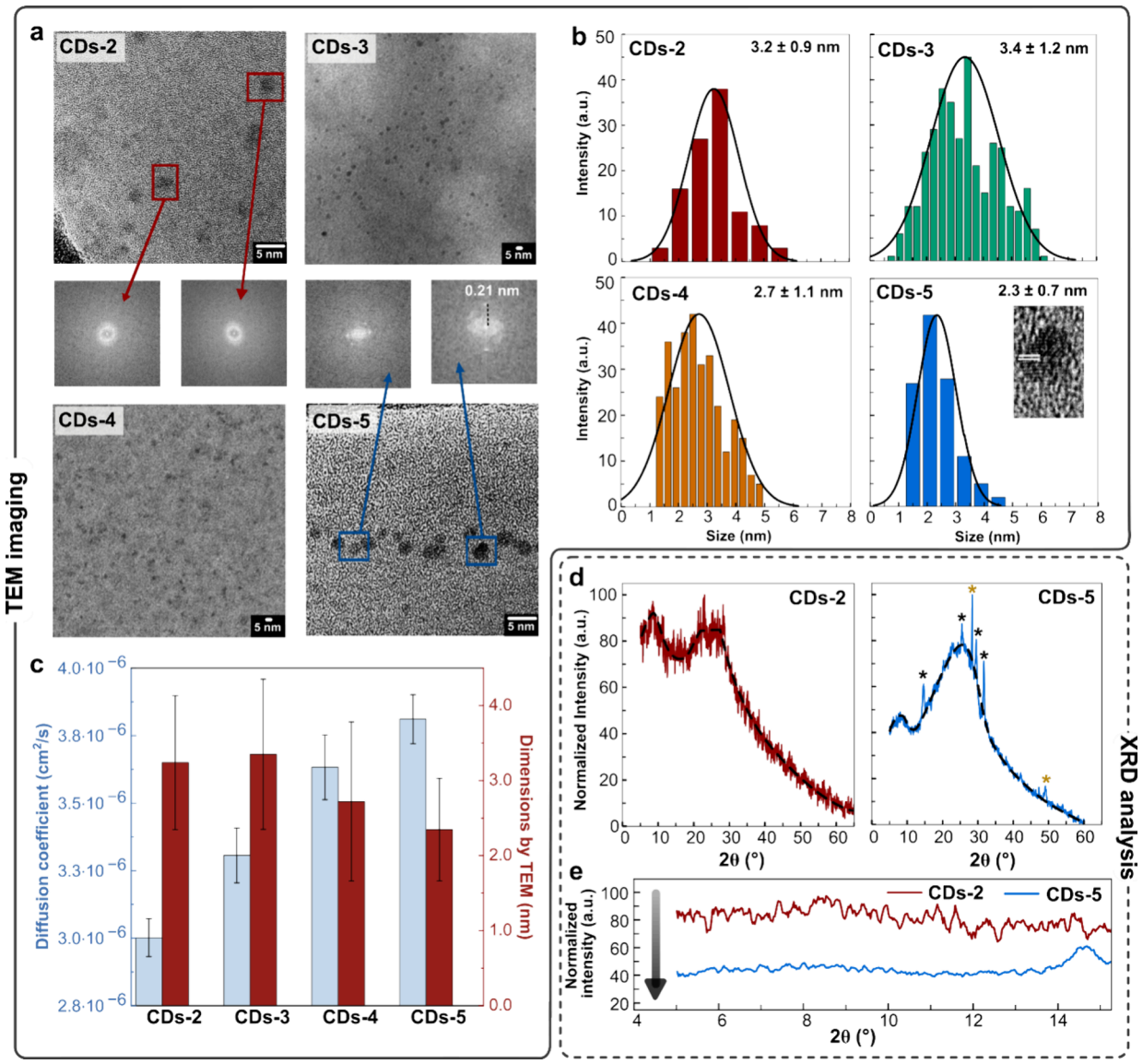

Figure 7. (a) TEM and HR-TEM images of CDs 2-5. (b) Plots showing the size distribution (fitted by a Gaussian curve) of samples CDs 2-5 calculated from TEM images. The errors reported are standard deviations. (c) Plot highlighting the relationship between the diffusion coefficients and diameter for samples CDs 2-5. Error bars represent the fitting errors. (d) XRD patterns of samples CDs-2 and CDs-5. Stars indicate minor impurities (black stars = calcium sulfate; reference code 00−043−0606; yellow stars = Ca salt; reference code 00−010−0348). Black dotted lines highlight the broad XRD diffraction peaks of the CDs. (e) Magnification of the spectral region referred to highly disordered amorphous carbon. The black arrow highlights the reduced contribution of amorphous carbon from CDs-2 to CDs-5.

As already discussed, the functional groups of the starting reagents can be retained in the **CD** structure, in particular, on their surfaces. Due to this, the characterization of the **CD** surface functional groups is indispensable to better understand their chemical properties. As the initial step of the characterization, **CDs** were investigated by means of X-ray Photoelectron Spectroscopy (XPS). In the XPS spectra of all the analyzed **CDs**, the carbon 1s signal, between 280 and 295 eV, was composed of four components associated with C−C/C═C at 284.8 eV, C−O/C−N at 286.6, C═O/C═N at 288.2 and O−C═O at 290.0 eV, confirming a variety of heteroatomic functionalities. The nitrogen 1s signal (395−405 eV) mainly consisted of the aminic component RN−H/NH_2 at 399.0 eV. Two other small contributions, attributed to the C═N bond and graphitic nitrogen, respectively, were centered at around 397.6 and 401.4 eV. Lastly, the oxygen 1s signal at 525−540 eV could be deconvoluted into two main components. The more predominant one at 531.4 eV was referred to C═O while the second, at 532.9 eV, was associated with the C−O moieties.[61−63] The results confirmed that all the **CDs** were mainly composed of carbon, nitrogen and oxygen (Survey spectra in Figure S25), with no significant differences between the batches. **CD** surface was also investigated with Fourier Transform Attenuated Total Reflectance (FT-ATR) spectroscopy. In the acquired spectra (Figure 8a), the peaks around 3400 cm^{-1} were assigned to the O−H/N−H stretching vibrations, while those near 1700 cm^{-1} suggest C═O stretching. Additionally, peaks around 1600 and 1400 cm^{-1} were ascribed to C═N/C═C and C−N bending vibrations respectively, while peaks at around 1150 cm^{-1} referred to C−O stretching. Taken together, these results confirmed the presence on the surface of **CDs** of functional groups mainly composed by oxygen and nitrogen.

https://doi.org/10.1021/acsnano.4c16538
ACS Nano 2025, 19, 4887−4900

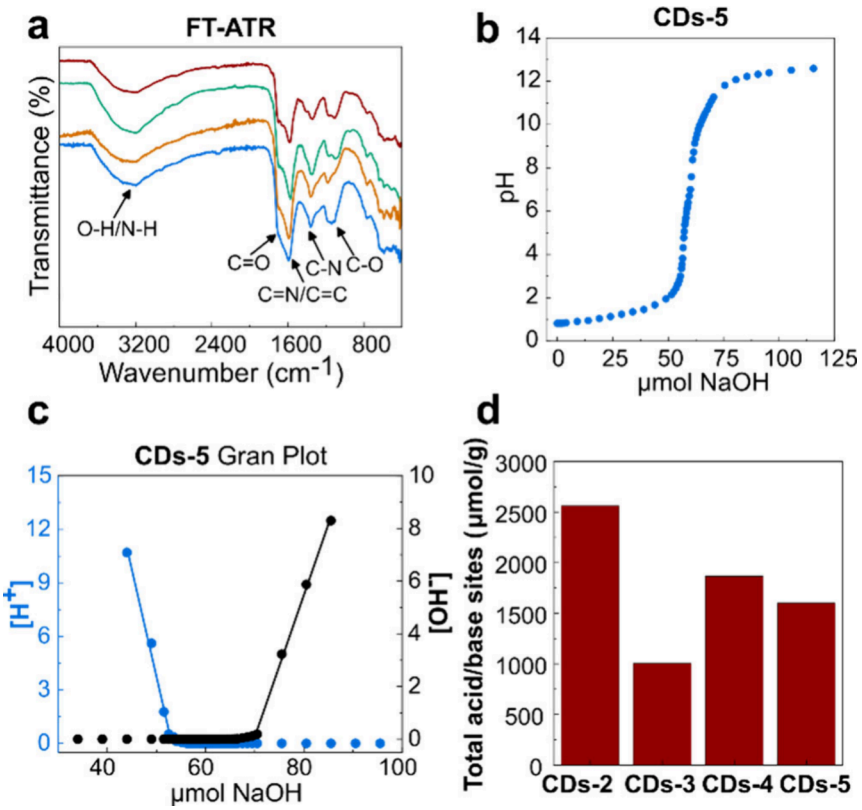

Figure 8. (a) FT-ATR spectra of CDs-2 (red line), CDs-3 (green line), CDs-4 (orange line), and CDs-5 (blue line). Samples were analyzed as powder. (b) Plot showing the pH titration curve of CDs-5. For the titration, a solution of 1.7 mg mL^{-1} of CDs-5 was acidified with 500 μL of 1 M HCl and then back-titrated with 0.1 M NaOH. (c) Gran Plot analysis of the CDs-5 titration in (b). (d) Percentage of acid/base sites on the surface of CDs 2-5.

We then proceeded to quantify these surface functional groups, evaluating the total number of acid and base sites on **CD** surface.[11,15] This was achieved by pH back-titration (Figure 8b), with subsequent data analysis employing Gran Plot analysis (Figure 8c and Figure S26).

By comparing the total number of acid/base sites on **CDs 2-5** (2562 μmol g^{-1}, 1005 μmol g^{-1}, 1866 μmol g^{-1} and 1600 μmol g^{-1} respectively) it was clear that the number of retained surface functionalities decreased as the synthesis conditions become harsher, and in particular when the synthesis time was increased (Figure 8d). This was due to the fact that the prolonged microwave heating brought to urea decomposition and citric acid decarboxylation and dehydration.[64,65] A comparison of the number of acid/base functionalities on the surface of the **CDs** with those associated with the starting materials allowed for the quantification of the acid/base sites retained during the synthesis, highlighting the same trend (Figure S27). In general, the increase in both synthesis time and temperature led to a reduction in the total amount of functional groups on the surface of **CDs**. However, how this affects their catalytic abilities is still an aspect under investigation. Nonetheless, an inverse relationship between **CD** graphitization and the amount of retained surface functional groups was clearly evidenced in this study.

CONCLUSIONS

In this work, we have shown that the catalytic performance of **CDs** is significantly influenced by the synthesis conditions. In particular, as confirmed by TEM and XRD analyses, it emerged that high synthesis temperatures induced graphitization of the **CD** core, while long synthesis times (at lower temperatures) led to amorphous materials. However, our experimental data showed that the graphitization of **CDs** has limitations. In fact, when the synthesis temperature was increased above a critical value (which is different for each synthesis protocol), the entire reaction mixture graphitized, resulting in insoluble bulk graphitic materials rather than discrete graphitic **CDs**. This was further proven by the fact that harsh synthetic conditions also resulted in a reduction of surface functional groups, indicating a trade-off between achieving higher graphitization, which is important for photocatalysis, and retaining surface functionalities. Based on this, we could conclude that the level of graphitization of the core of the **CDs** and the number of functional groups, which are important for both reactivity and solubility, are inversely proportional and depend on starting materials and synthetic protocols. In fact, these functionalities are crucial for **CD** solubility and can be used as anchoring points for their further functionalization and for the fabrication of nanocomposite materials.

We also showed that the **CDs** with higher graphitization (**CDs-5**) exhibit superior catalytic performance compared to the other **CDs**. The superior performance was attributed to the formation of more graphitic core structures under harsh synthesis conditions. In fact, as shown by the TEM imaging and XRD analysis, the core of the **CDs** mainly consists of (hetero)aromatic systems embedded in a matrix of amorphous carbon. It is reasonable to assume that, upon light irradiation, these aromatic systems reach their excited state and transfer the photoexcitation from the **CDs** to the substrate leading to the formation of radical intermediates.[8,66] Moreover, based on the literature, we could hypothesize that the key reactive

https://doi.org/10.1021/acsnano.4c16538
ACS Nano 2025, 19, 4887−4900

intermediates in the photocatalytic reaction were open-shell species that could be generated by electron transfer from the excited state of the (hetero)aromatic moieties in the core of **CDs** to the ground state of the substrate (**2a**).[67] This is supported by our experimental data, which show that the more graphitic **CDs** are, the better they are as photocatalysts. We could, therefore, conclude that the catalytic abilities of **CDs** are strongly dependent on the (hetero)aromatic structures in their cores. Furthermore, by comparing morphological studies and fluorescence lifetime decay, we could assume that the most graphitized **CDs** possessed more extended sp^2-hybridized carbon domains in their core and therefore progressively longer excited state lifetimes.

The higher degree of graphitization also resulted in **CDs** with an improved light absorption capacity, allowing for an effective photoexcitation of the photocatalysts. All of these features can facilitate the electron transfer from the **CDs** to the substrate in the reaction environment, thus boosting the photocatalytic performances of our **CDs**. Furthermore, due to the presence of a robust graphitic core, **CDs-5** proved to be resistant to photobleaching and recyclable over four catalytic cycles. Additionally, the analysis of both TEM and AFM data highlighted a reduction in the dimensions of the **CDs** with the increase in their synthesis time and temperature. This was further validated by the inverse relationship between the **CD** dimensions and the DOSY diffusion coefficients.

From a general perspective, in this study, we have highlighted the importance of pairing precise control over the **CD** synthesis conditions with effective purification and characterization methodologies. Our strategy paves the way to the detailed investigation of the relationship between structure and photocatalytic abilities of **CDs**. We expect these findings to be pivotal to the development of new **CDs** with tailored physical−chemical properties. This opens the possibility to exploit them not only as more economic and sustainable photocatalysts for fine chemical production or even for larger applications in the chemical industry but also for the development of new **CD**-based functional nanomaterials or nanomaterial composites.

EXPERIMENTAL SECTION

Materials. Citric acid (Sigma-Aldrich, 99%), Urea (Riedel-de Haen, 99.5%), carbon tetrabromide (Fluorochem, 98%), 1-hexene (Sigma-Aldrich, 97%) were used without further purification. Ethyl acetate normal grade, hexane normal grade and acetonitrile HPLC grade were purchased from Sigma-Aldrich and used without further purification. Silica gel 60 (0.040−0.063 mm) was purchased from Sigma-Aldrich. Flot-A-Lyzer dialysis tubes with molecular weight cutoff 100−500 Da and 500−1000 Da were purchased from Repligen; 3500 Da dialysis membranes were bought from Spectrum Laboratories. Ultrapure fresh water obtained from a Millipore water purification system (>18 MΩ Milli-Q, Millipore) was used in all experiments. D_2O was purchased from WVR chemicals, and $CDCl_3$ was purchased from Sigma-Aldrich.

Methods. *Synthesis of CDs.* The **CD** syntheses were performed on a CEM Discover-SP laboratory microwave. The **CDs** were obtained *via* irradiation of an aqueous solution of citric acid and urea (1:6 mol/mol ratio). Typically, citric acid (38 mg) and urea (72 mg) in Milli-Q water (100 μL) were heated in a laboratory microwave at 200 W at different times and temperatures (see table in Figure 2b). In the process of heating, the solution changed color from transparent to brownish. The darker colors appeared as a result of the increased synthesis time and temperatures (Figure 2c).

After synthesis, the crude reaction mixtures were diluted up to 10 mL with Milli-Q water and double-filtered through 0.45 and 0.1 μm polytetrafluoroethylene (PTFE) microporous membranes. The so-obtained solutions were dialyzed for 48 h (24 h against Milli-Q water containing 100 mM NaCl followed by 24 h against pure Milli-Q water). Finally, the purified products were lyophilized, giving deep brown solids.

^{1}H NMR and DOSY Experiments. The ^{1}H NMR spectra were recorded on a Varian 400 spectrometer (^{1}H: 400 MHz); the ^{13}C NMR and DOSY spectra were recorded on a Varian Inova 500 (^{1}H: 500 MHz; ^{13}C 125 MHz). The DOSY experiments were carried out using a Varian Inova 500 spectrometer with the following method: DOSY Gradient Compensated Stimulated Echo Spin Lock and Convection Compensation Experiment (DgcsteSL_cc). Diffusion gradient length = 1.4 ms, diffusion delay = 100 ms. DOSY spectra were deconvoluted from the raw data using a peak fit algorithm; diffusion coefficients were retrieved by exponential decay fitting of the intensity of the **CD** peaks. The spectra were analyzed and plotted using MestreNova − MestreLab software.

UV−vis and Fluorescence Spectroscopy. The UV−vis spectra were recorded on a PerkinElmer Lambda 35 UV−vis spectrophotometer. After an automatic blank subtraction, all of the UV−visible spectra were manually zeroed at 800 nm.

Fluorescence spectra were recorded on an Edinburgh Instruments FS5 spectrofluorometer. The emission spectra were automatically corrected by the instrument using an internal reference file.

All of the UV−vis and fluorescence spectra were recorded in Milli-Q water at room temperature using 1 cm path-length cuvettes. Numerical data were analyzed using Microsoft Excel and OriginLab software and plotted using OriginLab.

Atomic Force Microscopy (AFM) Imaging. The morphological characterization of the nanoparticles was carried out with a Multimode 8HR Atomic Force Microscope from Bruker. Images were acquired with Peak Force Tapping mode using a ScanAsyst-Air probe (Bruker). Deflection sensitivity was calibrated by a Thermal Tune. The images were acquired using a scan rate of 1 Hz, PF Amplitude at 150 nm, and PF Frequency of 2 kHz. The **CDs** were dissolved in Milli-Q at 0.001 mg mL^{-1}, sonicated and filtered (0.45 μm, hydrophilic PTFE filters). Then, 100 μL of the solutions was drop cast on freshly cleaved mica and dried overnight before the measurements. Images were processed using WSxM 5.0 software, measuring at least 100 nanoparticles in each image. Overall, 5 images were analyzed. Size distributions were analyzed using Microsoft Excel and OriginLab software and plotted using OriginLab.

Photocatalytic Reactions. The experiments were conducted at 20 °C in acetonitrile (0.25 M) in a sealed 10 mL Schlenk tube. Typically, 400 μL of acetonitrile (MeCN) HPLC grade, 12.5 μL of 1-hexene (**1a** 0.1 mmol), 66 mg of carbon tetrabromide (**2a** 0.2 mmol), and 3.5 mg of **CDs** were added at the bottom of the Schlenk tube. Before the reaction started, the Schlenk tube underwent three cycles of freeze−pump−thaw and was finally purged with argon. The reaction was then carried out for 16 h under light irradiation of a Kessil lamp with λ_{max} = 456 nm (50 W, Irradiance = 200 mW cm^{-2}). Control experiments were conducted to obtain more mechanistic clues about the reaction pathway. After the reaction, the crude reaction mixture was filtrated on a silica plug with ethyl acetate, dried overnight, and manually purified *via* flash chromatography (hexane was used as eluent). The corresponding product 1,1,1,3-tetrabromoheptane (**3a**) was obtained as a pale-yellow oil. See Figure S12 for all of the details of the experimental setup.

Stern−Volmer Quenching Studies. For these studies, a solution of 0.02 mg/mL of **CDs-5** was prepared in Milli-Q water/acetonitrile 1/1 as solvent. First, the emission spectrum of pristine **CDs-5** was recorded on an Edinburgh Instruments FS5 spectrofluorometer (λ_{exc} = 456 nm). Subsequently, increasing quantities of CBr_4 (quencher) were added to the solution. An emission spectrum was recorded after each addition. I_0/I was determined as relative fluorescence intensities at λ_{em} = 540 nm and plotted against the quencher concentration. The Stern−Volmer constant was retrieved by linear fitting according to eq 1:[52]

$$\frac{I_0}{I} = 1 + k_{SV}[Q] \quad (1)$$

All the fluorescence spectra were recorded at room temperature using 1 cm path-length cuvettes. During the acquisition, the spectra were automatically corrected by the instrument using an internal reference

https://doi.org/10.1021/acsnano.4c16538
ACS Nano 2025, 19, 4887−4900

file. Numerical data were analyzed using Microsoft Excel and OriginLab software, and plotted using OriginLab.

Extinction Coefficients Calculation. The calculation of the extinction coefficients can be a useful indication of the graphitization degrees of the **CDs**. To obtain these data, the **CDs** were solubilized in Milli-Q water, and multiple absorption spectra at different concentrations (mg mL^{-1}) were recorded. Subsequently, the absorbance value at 456 nm of the different concentrations was plotted, and the data were interpolated with a linear fitting. Finally, the extinction coefficient values were retrieved according to the Lambert−Beer by the slope of the interpolation line.[20] Extinction coefficients are reported in Figure 6a, and Figure S22 reports extinction coefficient spectra of **CDs 2-5**. The numerical values of the extinction coefficient spectra are reported in Appendix 1. Numerical data were analyzed using Microsoft Excel and OriginLab software and plotted using OriginLab.

Excited State Lifetimes (τ) Measurements. The fluorescence lifetimes were measured by time-correlated single-photon counting (TCSPC). For the measurements, an Edinburgh Instruments FS5 spectrofluorometer was equipped with an EPL-375 ps pulsed diode laser (Edinburgh Instruments). The instrumental signal was fitted with a double-exponential fit following eq 2.[68]

$$\text{Double exponential fitting} = A + B_1^{-t/\tau_1} + B_2^{-t/\tau_2} \quad (2)$$

All of the spectra were recorded in Milli-Q water at room temperature using 1 cm path-length cuvettes. Experimental data were analyzed using Microsoft Excel and OriginLab software and plotted using OriginLab.

Transmission Electron Microscopy (TEM) Imaging. TEM images were acquired with a JEOL JEM-1400 plus microscope with a LaB6 crystal operated at 80 kV. HR-TEM was performed with a JEOL JEM-2100F UHR running at 200 kV equipped with a 4 megapixel CMOS camera (TVIPS TemCam-F216). Samples for TEM and high-resolution HR-TEM were prepared by depositing 0.4 μL of **CDs** (5 mg mL^{-1} in water, HPLC grade) on a copper grid coated with a layer of ultrathin carbon film (01824, TED PELLA, INC.), which was freshly UV-ozone cleaned. Free software ImageJ was used to identify particles (>150 from different window views) and measure their size (largest diameter). Size distributions were analyzed using Microsoft Excel and OriginLab software, and plotted using OriginLab.

X-ray Diffraction (XRD). X-ray powder diffraction patterns were collected by using a Philips X'pert PRO automatic diffractometer operating at 40 kV and 40 mA, in theta−theta configuration, secondary monochromator with Cu−Kα radiation (λ = 1.5418 Å), and a PIXcel solid state detector (active length in 2θ = 3.347°). Data were collected from 5° to 60° 2θ, step size 0.026°/s, and time per step of 400 s at RT (total time 58 min, scan speed 0.0167°/s). 1° fixed soller and divergence slit giving a constant volume of sample illumination were used. To purify the **CDs** from calcium salts contamination, the pure **CD** samples were dialyzed against HPLC water (CHROMASOLV Plus, for HPLC - 34877) for 24 h, using a dialysis membrane with 500−1000 Da MWCO. The water was changed at least 4 times for each sample. Numerical data were analyzed using Microsoft Excel and OriginLab software, and plotted using OriginLab.

pH Titrations and Gran Plot Analysis. pH measurements were performed at 25 °C under continuous stirring using a data logging Seven Compact digital pH-meter equipped with an InLab semi-Micro electrode (Mettler Toledo). For the measurements aqueous solutions of **CDs** in Milli-Q water (1.7 mg mL^{-1}) were acidified with HCl 1 M (500 μL), and then titrated with NaOH 0.1 M. After titration, the acid/base sites on the **CDs** surface were quantified by means of Gran Plot analysis.[11,69] According to this procedure, the μmol of H^+ and OH^- present in the solution were plotted against the μmol of titrant added during the process. In the obtained graph, two linear regions could be individuated, allowing for the extrapolation of the amount of titrant at the equivalent points through a linear fitting. Finally, the number of acid/base active sites in 1 g of **CDs** was calculated according to eq 3.

$$\text{Acid/base sites (in 1 g)} = \frac{[H^+] - [OH^-]}{\text{CDs (g)}} \quad (3)$$

To calculate the amount of acid/base sites retained after the synthesis, the number of acid/base sites in 1 g of **CDs** was compared with the acid base sites in 1 g of the starting materials (eq 4).

$$\text{Retained acid/base sites (\%)} = \frac{\text{Retained acid/base sites}}{\text{Total acid/base sites}} \times 100 \quad (4)$$

Numerical data were analyzed using Microsoft Excel and OriginLab software, and plotted using OriginLab.

Fourier-Transform Infrared Spectroscopy. Fourier-Transform infrared spectroscopy was performed by the attenuated total reflection (ATR) method on a GladiATR instrument (Pike Technologies) equipped with a germanium crystal plate. A blank spectrum of the background was automatically subtracted by the instrument. The samples were deposited as a powder. Spectra were plotted without further analysis by using OriginLab software.

X-ray Photoelectron Spectroscopy (XPS). The chemical composition of the synthesized **CDs** was analyzed using the XPS technique. The experiments were performed in a Versaprobe III Physical Electronics (ULVAC) spectrometer with a monochromatic X-ray source (Aluminum Kα line of 1487 eV), calibrated using the 3d5/2 line of Ag at 368.26 eV. Samples, as powder, were mounted on no-conductive double-sided tape. E-neutralizer and Argon ion neutralizer were used for charge compensation. Z-alignment was performed for optimal sample height prior to each sample measurement. The elemental quantification was done on survey scan with step energy 0.5 eV, pass energy 224 eV, while high resolution regions were acquired with step energy 0.05 eV, pass energy 55 eV, time per step 50 ms. Raw data without further elaboration were analyzed by CasaXPS software (2.3.26 PR 1.0). Final curves were plotted using OriginLab software.

ASSOCIATED CONTENT

Supporting Information

The Supporting Information is available free of charge at https://pubs.acs.org/doi/10.1021/acsnano.4c16538.

Additional experimental details and supplementary figures, detailed description of **CD** dialysis water, photocatalytic experiments and **CD** characterization. (PDF)

Appendix 1: Numerical values of extinction coefficient spectra of **CDs 2−5** (PDF)

AUTHOR INFORMATION

Corresponding Authors

Maurizio Prato − *Department of Chemical and Pharmaceutical Sciences, INSTM UdR Trieste, University of Trieste, 34127 Trieste, Italy; Center for Cooperative Research in Biomaterials (CIC biomaGUNE), Basque Research and Technology Alliance (BRTA), Donostia-San Sebastián 20014, Spain; Ikerbasque, Basque Foundation for Science, Bilbao 48013, Spain;* orcid.org/0000-0002-8869-8612; Email: prato@units.it

Giacomo Filippini − *Department of Chemical and Pharmaceutical Sciences, INSTM UdR Trieste, University of Trieste, 34127 Trieste, Italy;* orcid.org/0000-0002-9694-3163; Email: gfilippini@units.it

Pierangelo Gobbo − *Department of Chemical and Pharmaceutical Sciences, INSTM UdR Trieste, University of Trieste, 34127 Trieste, Italy;* orcid.org/0000-0003-2575-5816; Email: pierangelo.gobbo@units.it

Authors

Laura Morbiato − *Department of Chemical and Pharmaceutical Sciences, INSTM UdR Trieste, University of Trieste, 34127 Trieste, Italy*

https://doi.org/10.1021/acsnano.4c16538
ACS Nano 2025, 19, 4887−4900

Lucia Cardo − *Center for Cooperative Research in Biomaterials (CIC biomaGUNE), Basque Research and Technology Alliance (BRTA), Donostia-San Sebastián 20014, Spain*
Elisa Sturabotti − *Center for Cooperative Research in Biomaterials (CIC biomaGUNE), Basque Research and Technology Alliance (BRTA), Donostia-San Sebastián 20014, Spain*

Complete contact information is available at:
https://pubs.acs.org/10.1021/acsnano.4c16538

Funding

European Research Council (ERC AdG-2019 n° 885323, e-DOTS; PROTOMAT − 101039578). University of Trieste, INSTM, Italian Ministry of Education MIUR (cofin Prot. 2017PBXPN4 and Prot. 20228YFRNL). FRA2024 funded by the University of Trieste and Microgrants 2024 funded by Region FVG (LR 2/2011, ART. 4).

Notes

The authors declare no competing financial interest.

ACKNOWLEDGMENTS

The authors thank M. Gallego Gonzalez of the Electron Microscopy platform at CICbiomaGUNE for her support during HR-TEM measurements. The authors also thank A. Larrañaga Varga from SGIker (UPV/EHU/ERDF, EU) for the technical support with XRD measurements. M. Prato and P. Gobbo thank the European Research Council (ERC AdG-2019 n° 885323, e-DOTS; PROTOMAT − 101039578). M. Prato is the AXA Chair for Bionanotechnology (2016−2026). Views and opinions expressed are however those of the authors only and do not necessarily reflect those of the European Union or the European Research Council. Neither the European Union nor the granting authority can be held responsible for them. The authors also gratefully acknowledge the University of Trieste, INSTM, Italian Ministry of Education MIUR (cofin Prot. 2017PBXPN4 and Prot. 20228YFRNL). G. Filippini kindly acknowledges FRA2024 funded by the University of Trieste and Microgrants 2024 funded by Region FVG (LR 2/2011, ART. 4).

REFERENCES

(1) Ravelli, D.; Dondi, D.; Fagnoni, M.; Albini, A. Photocatalysis. A Multi-Faceted Concept for Green Chemistry. *Chem. Soc. Rev.* **2009**, *38* (7), 1999−2011.
(2) Abderrazak, Y. Photocatalysis: A Step Closer to The Perfect Synthesis. *J. Organomet. Chem.* **2020**, *920*, 121335.
(3) Fresno, F.; Portela, R.; Suárez, S.; Coronado, J. M. Photocatalytic Materials: Recent Achievements and Near Future Trends. *J. Mater. Chem.* **2014**, *2* (9), 2863−2884.
(4) Srivastava, V.; Singh, P. K.; Singh, P. P. Recent Advances of Visible-Light Photocatalysis in The Functionalization of Organic Compounds. *J. Photochem. Photobiol.* **2022**, *50*, 100488.
(5) Twilton, J.; Le, C.; Zhang, P.; Shaw, M. H.; Evans, R. W.; MacMillan, D. W. C. The Merger of Transition Metals and Photocatalysis. *Nat. Rev. Chem.* **2017**, *1* (7), No. 0052.
(6) Zhu, Y. Y.; Lan, G.; Fan, Y.; Veroneau, S. S.; Song, Y.; Micheroni, D.; Lin, W. Merging Photoredox And Organometallic Catalysts in A Metal−Organic Framework Significantly Boosts Photocatalytic Activities. *Angew. Chem., Int. Ed.* **2018**, *57* (43), 14090−14094.
(7) Djurišić, A. B.; He, Y.; Ng, A. Visible-Light Photocatalysts: Prospects And Challenges. *APL. Mater.* **2020**, *8* (3), No. 030903.
(8) Sbacchi, M.; Mamone, M.; Morbiato, L.; Gobbo, P.; Filippini, G.; Prato, M. Shining Light on Carbon Dots: New Opportunities in Photocatalysis. *ChemCatChem.* **2023**, *15* (16), e202300667.
(9) Garrido, M.; Gualandi, L.; Di Noja, S.; Filippini, G.; Bosi, S.; Prato, M. Synthesis And Applications of Amino-Functionalized Carbon Nanomaterials. *ChemComm* **2020**, *56* (84), 12698−12716.
(10) Rosso, C.; Filippini, G.; Prato, M. Use of Nitrogen-Doped Carbon Nanodots for The Photocatalytic Fluoroalkylation of Organic Compounds. *Chem. - Eur. J.* **2019**, *25* (70), 16032−16036.
(11) Filippini, G.; Amato, F.; Rosso, C.; Ragazzon, G.; Vega-Peñaloza, A.; Companyó, X.; Dell'Amico, L.; Bonchio, M.; Prato, M. Mapping the Surface Groups of Amine-Rich Carbon Dots Enables Covalent Catalysis in Aqueous Media. *Chem.* **2020**, *6* (11), 3022−3037.
(12) Đorđevic, L.; Arcudi, F.; Cacioppo, M.; Prato, M. A Multifunctional Chemical Toolbox to Engineer Carbon Dots for Biomedical And Energy Applications. *Nat. Nanotechnol.* **2022**, *17* (2), 112−130.
(13) Barman, M. K.; Patra, A. Current Status and Prospects on Chemical Structure Driven Photoluminescence Behaviour of Carbon Dots. *J. Photochem. Photobiol.* **2018**, *37*, 1−22.
(14) Wang, B.; Lu, S. The Light of Carbon Dots: From Mechanism to Applications. *Matter* **2022**, *5* (1), 110−149.
(15) Gentile, G.; Mamone, M.; Rosso, C.; Amato, F.; Lanfrit, C.; Filippini, G.; Prato, M. Tailoring The Chemical Structure of Nitrogen-Doped Carbon Dots For Nano-Aminocatalysis in Aqueous Media. *ChemSusChem* **2023**, *16* (7), e202202399.
(16) Liu, H.; Zhong, X.; Pan, Q.; Zhang, Y.; Deng, W.; Zou, G.; Hou, H.; Ji, X. A review of Carbon Dots in Synthesis Strategy. *Coord. Chem. Rev.* **2024**, *498*, 215468.
(17) Rigodanza, F.; Burian, M.; Arcudi, F.; Đorđević, L.; Amenitsch, H.; Prato, M. Snapshots into Carbon Dots Formation Through A Combined Spectroscopic Approach. *Nat. Commun.* **2021**, *12* (1), 2640.
(18) Shi, L.; Yang, J. H.; Zeng, H. B.; Chen, Y. M.; Yang, S. C.; Wu, C.; Zeng, H.; Yoshihito, O.; Zhang, Q. Carbon Dots with High Fluorescence Quantum Yield: The Fluorescence Originates from Organic Fluorophores. *Nanoscale* **2016**, *8* (30), 14374−14378.
(19) Xiong, Y.; Schneider, J.; Ushakova, E. V.; Rogach, A. L. Influence of Molecular Fluorophores on The Research Field of Chemically Synthesized Carbon Dots. *Nano Today* **2018**, *23*, 124−139.
(20) Mintz, K. J.; Bartoli, M.; Rovere, M.; Zhou, Y.; Hettiarachchi, S. D.; Paudyal, S.; Chen, J.; Domena, J. B.; Liyanage, P. Y.; Sampson, R. A Deep Investigation into The Structure of Carbon Dots. *Carbon* **2021**, *173*, 433−447.
(21) Niu, K.-K.; Ma, C.-Q.; Dong, R.-Z.; Liu, H.; Yu, S.-S.; Xing, L.-B. Nitrogen-Doped Carbon Dots As Photocatalysts for Organic Synthesis: Effect of Nitrogen Content on Catalytic Activity. *Nano Res.* **2024**, *17*, 4825−4833.
(22) Bartolomei, B.; Bogo, A.; Amato, F.; Ragazzon, G.; Prato, M. Nuclear Magnetic Resonance Reveals Molecular Species in Carbon Nanodot Samples Disclosing Flaws. *Angew. Chem., Int. Ed.* **2022**, *61* (20), e202200038.
(23) Di Noja, S.; Amato, F.; Zinna, F.; Di Bari, L.; Ragazzon, G.; Prato, M. Transfer of Axial Chirality to The Nanoscale Endows Carbon Nanodots with Circularly Polarized Luminescence. *Angew. Chem., Int. Ed.* **2022**, *134* (26), e202202397.
(24) Bartolomei, B.; Prato, M. The Importance of The Purification Step And The Characterization of The Products in The Synthesis of Carbon Nanodots. *Small* **2023**, *19* (31), 2206714.
(25) Groves, P. Diffusion Ordered Spectroscopy (DOSY) As Applied to Polymers. *Polym. Chem.* **2017**, *8* (44), 6700−6708.
(26) Cardo, L.; Martinez-Parra, L.; Cesco, M.; Echeverria-Beistegui, B. M.; Martinez-Moro, M.; Herrero-Alvarez, N.; Cabrerizo, M.-B.; Carregal-Romero, S.; Ramos-Cabrer, P.; Ruiz-Cabello, J.; Prato, M. Luminescent Carbon Nanodots Doped with Gadolinium (III): Purification Criteria, Chemical And Biological Characterization of A New Dual Fluorescence/MR Imaging Agent. *Small* **2023**, *19* (31), 2206442.
(27) Xu, X.; Ray, R.; Gu, Y.; Ploehn, H. J.; Gearheart, L.; Raker, K.; Scrivens, W. A. Electrophoretic Analysis and Purification of Fluorescent Single-Walled Carbon Nanotube Fragments. *J. A. C. S.* **2004**, *126* (40), 12736−12737.

(28) Zhu, S.; Song, Y.; Zhao, X.; Shao, J.; Zhang, J.; Yang, B. The Photoluminescence Mechanism in Carbon Dots (Graphene Quantum Dots, Carbon Nanodots, and Polymer Dots): Current State and Future Perspective. *Nano Res.* **2015**, *8*, 355−381.
(29) Kelarakis, A. From Highly Graphitic to Amorphous Carbon Dots: A Critical Review. *MRS Energy Sustain.* **2014**, *1*, E2.
(30) Xia, C.; Zhu, S.; Feng, T.; Yang, M.; Yang, B. Evolution And Synthesis of Carbon Dots: From Carbon Dots to Carbonized Polymer Dots. *Adv. Sci.* **2019**, *6* (23), 1901316.
(31) Miao, X.; Qu, D.; Yang, D.; Nie, B.; Zhao, Y.; Fan, H.; Sun, Z. Synthesis of Carbon Dots with Multiple Color Emission by Controlled Graphitization And Surface Functionalization. *Adv. Mater.* **2018**, *30* (1), 1704740.
(32) Manoj, B.; Kunjomana, A. G. Study of Stacking Structure of Amorphous Carbon by X-Ray Diffraction Technique. *Int. J. Electrochem. Sci.* **2012**, *7* (4), 3127−3134.
(33) Hu, Y.; Yang, J.; Tian, J.; Yu, J.-S. How do Nitrogen-Doped Carbon Dots Generate from Molecular Precursors? An Investigation of The Formation Mechanism and A Solution-Based Large-Scale Synthesis. *J. Mater. Chem. B* **2015**, *3* (27), 5608−5614.
(34) Bianchi, P.; Williams, J. D.; Kappe, C. O. Continuous Flow Processing of Bismuth-Photocatalyzed Atom Transfer Radical Addition Reactions Using An Oscillatory Flow Reactor. *Green Chem.* **2021**, *23* (7), 2685−2693.
(35) Courant, T.; Masson, G. Recent Progress in Visible-Light Photoredox-Catalyzed Intermolecular 1,2-Difunctionalization of Double Bonds via An ATRA-Type Mechanism. *J. Org. Chem.* **2016**, *81* (16), 6945−6952.
(36) Strauss, V.; Wang, H.; Delacroix, S.; Ledendecker, M.; Wessig, P. Carbon Nanodots Revised: The Thermal Citric Acid/Urea Reaction. *Chem. Sci.* **2020**, *11* (31), 8256−8266.
(37) Zhou, Y.; Mintz, K. J.; Sharma, S. K.; Leblanc, R. M. Carbon Dots: Diverse Preparation, Application, And Perspective in Surface Chemistry. *Langmuir* **2019**, *35* (28), 9115−9132.
(38) Krysmann, M. J.; Kelarakis, A.; Dallas, P.; Giannelis, E. P. Formation Mechanism of Carbogenic Nanoparticles With Dual Photoluminescence Emission. *J. A. C. S.* **2012**, *134* (2), 747−750.
(39) Hamadamin, A.; Benazzi, V.; Campalani, C.; Quattri, L.; Ravelli, D.; Hussain, F.; Perosa, A.; Selva, M.; Protti, S. Nitrogen-Doped Carbon Dots As Biobased Catalysts for Visible Light Driven 1,2-Functionalization of Olefins through An Atom Transfer Radical Addition Process. *ChemCatChem.* **2023**, *15* (17), e202300708.
(40) Mandal, S.; Das, P. Are Carbon Dots Worth The Tremendous Attention It Is Getting: Challenges And Opportunities. *Appl. Mater. Today* **2022**, *26*, 101331.
(41) Essner, J. B.; Kist, J. A.; Polo-Parada, L.; Baker, G. A. Artifacts and Errors Associated with The Ubiquitous Presence of Fluorescent Impurities in Carbon Nanodots. *Chem. Mater.* **2018**, *30* (6), 1878−1887.
(42) Luo, H.; Papaioannou, N.; Salvadori, E.; Roessler, M. M.; Ploenes, G.; van Eck, E. R. H.; Tanase, L. C.; Feng, J.; Sun, Y.; Yang, Y. Manipulating The Optical Properties of Carbon Dots by Fine-Tuning Their Structural Features. *ChemSusChem* **2019**, *12* (19), 4432−4441.
(43) Hu, S.; Tian, R.; Dong, Y.; Yang, J.; Liu, J.; Chang, Q. Modulation and Effects of Surface Groups on Photoluminescence and Photocatalytic Activity of Carbon Dots. *Nanoscale* **2013**, *5* (23), 11665−11671.
(44) van Dam, B.; Nie, H.; Ju, B.; Marino, E.; Paulusse, J. M. J.; Schall, P.; Li, M.; Dohnalová, K. Excitation-Dependent Photoluminescence from Single-Carbon Dots. *Small* **2017**, *13* (48), 1702098.
(45) Zhang, Y.; Wang, Y.; Feng, X.; Zhang, F.; Yang, Y.; Liu, X. Effect of Reaction Temperature on Structure and Fluorescence Properties of Nitrogen-Doped Carbon Dots. *Appl. Surf. Sci.* **2016**, *387*, 1236−1246.
(46) Sarkar, S.; Sudolska, M.; Dubecky, M.; Reckmeier, C. J.; Rogach, A. L.; Zboril, R.; Otyepka, M. Graphitic Nitrogen Doping in Carbon Dots Causes Red-Shifted Absorption. *J. Phys. Chem. C* **2016**, *120* (2), 1303−1308.
(47) Song, Y.; Zhu, S.; Zhang, S.; Fu, Y.; Wang, L.; Zhao, X.; Yang, B. Investigation From Chemical Structure to Photoluminescent Mechanism: A Type of Carbon Dots from The Pyrolysis of Citric Acid and An Amine. *J. Mater. Chem. C* **2015**, *3* (23), 5976−5984.
(48) Wang, Z.; Zhang, Z.; Wu, C.; Wang, Z.; Liu, W. Pushing the Limit of Photo-Controlled Polymerization: Hyperchromic and Bathochromic Effects. *Mol.* **2024**, *29* (10), 2377.
(49) Holá, K.; Sudolská, M.; Kalytchuk, S.; Nachtigallová, D.; Rogach, A. L.; Otyepka, M.; Zbořil, R. Graphitic Nitrogen Triggers Red Fluorescence in Carbon Dots. *ACS Nano* **2017**, *11* (12), 12402−12410.
(50) Datta, P.; Roy, D.; Jain, D.; Kumar, S.; Sil, S.; Bhunia, A.; Dasgupta, J.; Mandal, S. K. Uncovering The On-Pathway Reaction Intermediates for Metal-Free Atom Transfer Radical Addition to Olefins through Photogenerated Phenalenyl Radical Anion. *ACS Catal.* **2024**, *14* (5), 3420−3433.
(51) Barham, J. P.; Coulthard, G.; Emery, K. J.; Doni, E.; Cumine, F.; Nocera, G.; John, M. P.; Berlouis, L. E. A.; McGuire, T.; Tuttle, T.; Murphy, J. A. KOtBu: A Privileged Reagent for Electron Transfer Reactions? *J. A. C. S.* **2016**, *138* (23), 7402−7410.
(52) Buzzetti, L.; Crisenza, G. E. M.; Melchiorre, P. Mechanistic Studies in Photocatalysis. *Angew. Chem., Int. Ed.* **2019**, *58* (12), 3730−3747.
(53) Liu, Y.; Liu, C.-Y.; Zhang, Z.-Y. Graphitized Carbon Dots Emitting Strong Green Photoluminescence. *J. Mater. Chem. C* **2013**, *1* (32), 4902−4907.
(54) Muhammad, S.; Xu, H.-L.; Zhong, R.-L.; Su, Z.-M.; Al-Sehemi, A. G.; Irfan, A. Quantum Chemical Design of Nonlinear Optical Materials by sp2-Hybridized Carbon Nanomaterials: Issues and Opportunities. *J. Mater. Chem. C* **2013**, *1* (35), 5439−5449.
(55) Xu, J.; Sahu, S.; Cao, L.; Bunker, C. E.; Peng, G.; Liu, Y.; Fernando, K. A. S.; Wang, P.; Guliants, E. A.; Meziani, M. J. Efficient Fluorescence Quenching in Carbon Dots by Surface-Doped Metals-Disruption of Excited State Redox Processes and Mechanistic Implications. *Langmuir* **2012**, *28* (46), 16141−16147.
(56) Mondal, S.; Yucknovsky, A.; Akulov, K.; Ghorai, N.; Schwartz, T.; Ghosh, H. N.; Amdursky, N. Efficient Photosensitizing Capabilities And Ultrafast Carrier Dynamics of Doped Carbon Dots. *J. A. C. S.* **2019**, *141* (38), 15413−15422.
(57) LeCroy, G. E.; Fernando, S. K. A.; Bunker, C. E.; Wang, P.; Tomlinson, N.; Sun, Y.-P. Steady-State and Time-Resolved Fluorescence Studies on Interactions of Carbon "Quantum" Dots with Nitrotoluenes. *Inorg. Chim. Acta* **2017**, *468*, 300−307.
(58) Boukhvalov, D. W.; Osipov, V. Y.; Murzalinov, D.; Serikkanov, A.; Bi, H. A Comprehensive Model of Carbon Nanodots with 0.21 nm Lattice Fringes Patterns. *Carbon* **2024**, *225*, 119101.
(59) Popova, A. N. Crystallographic Analysis of Graphite by X-Ray Diffraction. *Coke Chem.* **2017**, *60*, 361−365.
(60) Li, L.; Wu, G.; Yang, G.; Peng, J.; Zhao, J.; Zhu, J.-J. Focusing on Luminescent Graphene Quantum Dots: Current Status and Future Perspectives. *Nanoscale* **2013**, *5* (10), 4015−4039.
(61) Stachowska, J. D.; Murphy, A.; Mellor, C.; Fernandes, D.; Gibbons, E. N.; Krysmann, M. J.; Kelarakis, A.; Burgaz, E.; Moore, J.; Yeates, S. G. A Rich Gallery of Carbon Dots Based Photoluminescent Suspensions And Powders Derived by Citric Acid/Urea. *Sci. Rep.* **2021**, *11* (1), 10554.
(62) Egorova, M.; Kapitonov, A.; Alekseev, A.; Obraztsova, E. Properties of Carbon Dots Synthesized Solvothermally From Citric Acid And Urea. *J. Struct. Chem.* **2020**, *61*, 811−817.
(63) Emanuele, A.; Cailotto, S.; Campalani, C.; Branzi, L.; Raviola, C.; Ravelli, D.; Cattaruzza, E.; Trave, E.; Benedetti, A.; Selva, M.; Perosa, A. Precursor-Dependent Photocatalytic Activity of Carbon Dots. *Mol.* **2020**, *25* (1), 101.
(64) Schaber, P. M.; Colson, J.; Higgins, S.; Thielen, D.; Anspach, B.; Brauer, J. Thermal Decomposition (Pyrolysis) of Urea in An Open Reaction Vessel. *Thermochim. Acta* **2004**, *424* (1−2), 131−142.
(65) Ludmerczki, R.; Mura, S.; Carbonaro, C. M.; Mandity, I. M.; Carraro, M.; Senes, N.; Garroni, S.; Granozzi, G.; Calvillo, L.; Marras, S. Carbon Dots from Citric Acid And its Intermediates Formed by Thermal Decomposition. *Chem. - Eur. J.* **2019**, *25* (51), 11963−11974.

https://doi.org/10.1021/acsnano.4c16538
ACS Nano 2025, 19, 4887−4900

(66) Ragazzon, G.; Cadranel, A.; Ushakova, E. V.; Wang, Y.; Guldi, D. M.; Rogach, A. L.; Kotov, N. A.; Prato, M. Optical Processes in Carbon Nanocolloids. *Chem.* **2021**, *7* (3), 606−628.
(67) Rant, U.; Scherf, U.; Rehahn, M.; Galda, P.; Brédas, J. L.; Zojer, E. Influence of The Degree of Conjugation on Excited State Lifetimes In Phenylene-Based Materials. *Synth. Met.* **2002**, *127* (1), 241−245.
(68) Anilkumar, P.; Wang, X.; Cao, L.; Sahu, S.; Liu, J.-H.; Wang, P.; Korch, K.; Tackett, K. N., Ii; Parenzan, A.; Sun, Y.-P. Toward Quantitatively Fluorescent Carbon-Based "Quantum" Dots. *Nanoscale* **2011**, *3* (5), 2023−2027.
(69) Boiani, J. A. The Gran Plot Analysis of An Acid Mixture: An Undergraduate Experiment to Highlight This Alternate Method. *J. Chem. Educ.* **1986**, *63* (8), 724.

https://doi.org/10.1021/acsnano.4c16538
ACS Nano 2025, 19, 4887−4900